NIH Public Access
Author Manuscript
Magn Reson Med. Author manuscript; available in PMC 2011 October 1.

Published in final edited form as:
Magn Reson Med. 2010 October ; 64(4): 1057–1067. doi:10.1002/mrm.22497.

A Robust Methodology for In Vivo T_1 Mapping

Joëlle K. Barral[1], **Erik Gudmundson**[2], **Nikola Stikov**[1], **Maryam Etezadi-Amoli**[1], **Petre Stoica**[2], and **Dwight G. Nishimura**[1]

[1]Magnetic Resonance Systems Research Laboratory, Department of Electrical Engineering, Stanford University, Stanford, California

[2]Systems and Control Division, Department of Information Technology, Uppsala University, Uppsala, Sweden

Introduction

The T_1 parameter is an intrinsic MR property of tissue, and mapping T_1 in vivo is useful in several ways. First, knowledge of T_1 helps in optimizing the MR protocol, e.g., by setting the Ernst angle appropriately. In addition, it provides a tool to evaluate contrast uptake, blood perfusion and volume, as well as disease progression during a longitudinal study. Furthermore, it is often desirable to compare T_1 measurements across subjects and across scanners. While there are many techniques for T_1 mapping (1), there is also a wide range of reported T_1 values in tissue (2), an inconsistency that raises the issue of reproducibility and standardization.

The gold standard for T_1 mapping was developed from NMR experiments performed in the late 1940s (3,4). The method is known as inversion recovery T_1 mapping (IR), and it consists of inverting the longitudinal magnetization M_z and sampling the MR signal as it recovers with an exponential recovery time T_1. Different models have been used for T_1 mapping (1). With all models, the fit is traditionally performed using a Levenberg-Marquardt (LM) algorithm (5). Many methods have been proposed to speed up the scanning and fitting procedures, at the expense of accuracy and precision.

In this paper, we first justify the need for a four-parameter model when accurate T_1 mapping is desired. We show that this model is equivalent in terms of accuracy and precision of the T_1 estimation to a more general five-parameter model. We propose to solve a nonlinear least squares (NLS) problem to fit complex data to the five-parameter model. The problem is reduced to a search over one dimension, which substantially decreases the computational complexity. When only magnitude data are available, the algorithm is adapted to concurrently restore polarity. We perform Monte-Carlo simulations to compare the proposed algorithms to the conventional LM algorithm and to evaluate the influence of signal-to-noise ratio (SNR) on fitting performance. We then define a robust methodology for in vivo T_1 mapping. The method is validated with phantom scans and applied to brain and skin imaging.

Address correspondence to: Joëlle Barral, Packard Electrical Engineering, Room 211, 350 Serra Mall, Stanford, CA 94305-9510, TEL: (650) 804-6071, jbarral@mrsrl.stanford.edu.

NIH-PA Author Manuscript
NIH-PA Author Manuscript
NIH-PA Author Manuscript

NIH-PA Author Manuscript
NIH-PA Author Manuscript
NIH-PA Author Manuscript

1 Theory

1.1 Models

Let us recall the signal equations for the gradient-echo inversion recovery (GRE-IR) and spin-echo inversion recovery (SE-IR) sequences. We first consider the GRE-IR sequence $\{\theta_1 — TI — \theta_2 — (TR - TI)\}$, where θ_1 and θ_2 are the RF pulses, typically prescribed as 180° and 90°, respectively; *TI* is the inversion time; and *TR* the repetition time. If we assume instantaneous pulses, perfect spoiling of M_{xy} after θ_1, and no off-resonance effects, then (6):

$$M_z = M_0 \frac{1 - \cos(\theta_1) e^{-\frac{TR}{T_1}} - [1 - \cos(\theta_1)] e^{-\frac{TI}{T_1}}}{1 - \cos(\theta_1)\cos(\theta_2) e^{-\frac{TR}{T_1}}}. \quad (1)$$

Similarly, for a SE-IR sequence $\{\theta_1 — TI — \theta_2 — TE/2 — \theta_3 — (TR - TI - TE/2)\}$, where θ_3 is prescribed as 180°, and *TE* is the echo time, if the same assumptions are made, then (7):

$$M_z = M_0 \frac{1 - \cos(\theta_1)\cos(\theta_3) e^{-\frac{TR}{T_1}} - \cos(\theta_1)[1 - \cos(\theta_3)] e^{-\frac{TR - \frac{TE}{2}}{T_1}} - [1 - \cos(\theta_1)] e^{-\frac{TI}{T_1}}}{1 - \cos(\theta_1)\cos(\theta_2)\cos(\theta_3) e^{-\frac{TR}{T_1}}}. \quad (2)$$

Therefore, for both sequences, sampling the magnetization M_z at different inversion times TI_n leads to the following data equation for the received signal:

$$S(TI_n) = K M_z = e^{i\phi}\left(r_a + r_b e^{-\frac{TI_n}{T_1}}\right), \quad (3)$$

where

$$r_a = \begin{cases} |K| M_0 \frac{1 - \cos(\theta_1) e^{-\frac{TR}{T_1}}}{1 - \cos(\theta_1)\cos(\theta_2) e^{-\frac{TR}{T_1}}} & \text{for GRE–IR,} \\ |K| M_0 \frac{1 - \cos(\theta_1)\cos(\theta_3) e^{-\frac{TR}{T_1}} - \cos(\theta_1)[1 - \cos(\theta_3)] e^{-\frac{TR - \frac{TE}{2}}{T_1}}}{1 - \cos(\theta_1)\cos(\theta_2)\cos(\theta_3) e^{-\frac{TR}{T_1}}} & \text{for SE–IR,} \end{cases} \quad (4)$$

$$r_b = \begin{cases} -|K| M_0 \frac{1 - \cos(\theta_1)}{1 - \cos(\theta_1)\cos(\theta_2) e^{-\frac{TR}{T_1}}} & \text{for GRE–IR,} \\ -|K| M_0 \frac{1 - \cos(\theta_1)}{1 - \cos(\theta_1)\cos(\theta_2)\cos(\theta_3) e^{-\frac{TR}{T_1}}} & \text{for SE–IR,} \end{cases} \quad (5)$$

and $\phi \in [-\pi, \pi)$ is the phase of *K*, which has contributions from T_2 (SE–IR) or T_2^* (GRE-IR) and coil sensitivity. The model in Eq. 3 therefore has four real-valued unknown parameters: ϕ, r_a, r_b, and T_1.

We will also consider the following overparametrization of the model in Eq. 3, which will turn out to be useful mathematically:

NIH-PA Author Manuscript

NIH-PA Author Manuscript

NIH-PA Author Manuscript

$$S(TI_n)=a+be^{-\frac{TI_n}{T_1}}, \quad (6)$$

where a and b are complex-valued parameters. This model has five unknown real-valued parameters: Re{a}, Im{a}, Re{b}, Im{b}, and T_1, where Re{x} and Im{x} denote the real part and imaginary part of x, respectively. Equation 6 with $a = e^{i\phi}r_a$ and $b = e^{i\phi}r_b$—i.e., if a and b are assumed to have the same phase ϕ—reduces to Eq. 3.

Sampling the magnetization at three time points provides six equations, which are sufficient for T_1 estimation. More time points are often used to improve the quality of fit over the range of expected T_1 values.

Equations 1 and 2 can be simplified to a different four-parameter model if $TR \gg T_1$

$$S(TI_n)=c\left(1-[1-\cos(\theta_1)]e^{-\frac{TI_n}{T_1}}\right) \quad (7)$$

or to a three-parameter model if $TR \gg T_1$ and $\theta_1 = 180°$

$$S(TI_n)=c\left(1-2e^{-\frac{TI_n}{T_1}}\right), \quad (8)$$

where c is complex-valued.

A drawback with using Eq. 7 instead of Eq. 3 or Eq. 6 is that it assumes $TR \gg T_1$ and perfect knowledge of TI_n. TI_n is usually defined as the time between the middle of the inversion pulse θ_1 and the middle of the imaging pulse θ_2. However, inversion is not complete until the end of the inversion pulse. This systematic error is not a problem in Eq. 3 or Eq. 6, as it is absorbed in the parameter r_b or b. Another drawback of Eq. 7 is that the limited range of the cosine function introduces a bias in the estimation of θ_1, which is an issue for θ_1 close to 180° in the presence of noise or imperfections (2).

The three-parameter model in Eq. 8 is attractive since the LM fitting procedure is much faster when the number of parameters is reduced. Furthermore, the variance of the estimate of T_1 is usually expected to decrease (8–10). However, beyond the requirement that $TR \gg T_1$, the three-parameter model assumes a perfect inversion pulse (180°), an assumption that is rarely valid. Even if an adiabatic RF pulse is used, the effective flip angle will depend on both T_1 and T_2 (11). In addition, transition bands of the inversion profile are often partially included in the imaging slice to enable multi-slice imaging, and the effective flip angle should be taken as the integral of the inversion profile over the slice thickness. Using the three-parameter model, imperfections in the inversion profile can result in significant T_1 variations (7,12). Adiabatic RF pulses should still be preferred; even if they do not provide a perfect 180°, they get as close as possible to it and, therefore, maximize the available dynamic range and hence the SNR.

With these considerations in mind, we focus on the four- and five-parameter models in Eqs. 3 and 6. Interestingly enough, the Cramér-Rao Lower Bounds (CRLB)[1] of the T_1 estimate obtained using the four-parameter model in Eq. 3 and using the five-parameter model in Eq.

[1]The CRLB gives an expression, asymptotically in SNR or number of samples, for the minimum variance of an unbiased parameter estimate (13).

NIH-PA Author Manuscript

NIH-PA Author Manuscript

NIH-PA Author Manuscript

6 are identical (cf. Appendix A). Consequently, the variances of the T_1 estimate from these two models are expected to be very similar.

1.2 Fitting Procedures

Specific fitting procedures were derived for handling complex data and magnitude data. For complex data, the use of the five-parameter model in Eq. 6 allows the derivation of a fast fitting procedure. Monte-Carlo simulations then show that the proposed algorithm reaches the CRLBs, therefore the phase constraint on a and b improves neither the accuracy nor the precision in T_1 estimation. For magnitude data, the phase constraint is needed to restore polarity.

1.2.1 Complex Data—If complex data are available, Eq. 6 can be used directly. The unknown parameters $a \in \mathbb{C}$, $b \in \mathbb{C}$, and $T_1 \in \mathbb{R}$ can be estimated as the minimizers of the fitting criterion

$$J_1 = \sum_{n=1}^{N} \left| S(TI_n) - \left(a + be^{-\frac{TI_n}{T_1}} \right) \right|^2, \tag{9}$$

where N is the number of sampling points. Equation 9 is traditionally solved using the LM algorithm, which requires a five-dimensional search with proper initialization. The fit is therefore computationally demanding. In this work, we instead propose a reduced-dimension NLS (RD-NLS) approach to solve Eq. 9 (13), which allows for a separation of the unknown variables in J_1. The estimates, denoted by ^, are then obtained as (cf. Appendix B for details)

$$\widehat{T}_1 = \arg\max_{T_1} \frac{\left|\Gamma(T_1)\right|^2}{\Psi(T_1)}, \tag{10}$$

$$\widehat{b} = \frac{\Gamma(\widehat{T}_1)}{\Psi(\widehat{T}_1)}, \tag{11}$$

$$\widehat{a} = \frac{1}{N} \left(\sum_{n=1}^{N} S(TI_n) - \widehat{b} \sum_{n=1}^{N} e^{-\frac{TI_n}{\widehat{T}_1}} \right), \tag{12}$$

where

$$\Gamma(T_1) = \sum_{n=1}^{N} e^{-\frac{TI_n}{T_1}} S(TI_n) - \frac{1}{N} \left(\sum_{n=1}^{N} e^{-\frac{TI_n}{T_1}} \right) \left(\sum_{n=1}^{N} S(TI_n) \right), \tag{13}$$

$$\Psi(T_1) = \sum_{n=1}^{N} e^{-\frac{2TI_n}{T_1}} - \frac{1}{N} \left(\sum_{n=1}^{N} e^{-\frac{TI_n}{T_1}} \right)^2. \tag{14}$$

NIH-PA Author Manuscript

NIH-PA Author Manuscript

NIH-PA Author Manuscript

T_1 is therefore obtained through a one-dimensional (1D) search, and the remaining parameters are given in closed form.

We could use a similar approach for the model in Eq. 3, but the necessary calculations and the resulting algorithm are more involved than those corresponding to the model in Eq. 6. Owing to this reason and to the fact that there is no statistical performance gain associated with using the model in Eq. 3 compared to using the model in Eq. 6 (cf. Appendix A, where the CRLBs for the different models are derived and compared), we did not pursue the idea of getting an RD-NLS algorithm for the model in Eq. 3.

1.2.2 Magnitude Data—If only magnitude data are available, Eq. 3 becomes

$$y(TI) \triangleq |S(TI)| = \left| r_a + r_b e^{-\frac{TI}{T_1}} \right|, \tag{15}$$

leaving us with three unknowns: $r_a \in \mathbb{R}$, $r_b \in \mathbb{R}$, and $T_1 \in \mathbb{R}$. Using the model in Eq. 15 to estimate the unknowns would not be a simple task since the minimization criterion would not be differentiable everywhere. A remedy for this would be to use the square of the data, yielding the following NLS minimization criterion:

$$J_2 = \sum_{n=1}^{N} \left[y^2(TI_n) - \left(r_a + r_b e^{-\frac{TI_n}{T_1}} \right)^2 \right]^2. \tag{16}$$

Regrettably, there is no straightforward derivation of an RD-NLS-type algorithm for Eq. 16. However, as we assume $r_a + r_b e^{-\frac{TI}{T_1}}$ to be a monotonically increasing function in *TI* (Eqs. 4 and 5), we instead propose a technique that combines polarity restoration, a method commonly used to preserve noise statistics (14–17), and the RD-NLS approach in Sec. 1.2.1. The estimation method, called RD-NLS-PR (RD-NLS with polarity restoration), is outlined as follows.

Let the sign-shifting function γ be defined as

$$\gamma_\tau(TI) = \begin{cases} 1 & \text{if } TI \geq \tau, \\ -1 & \text{if } TI < \tau, \end{cases} \tag{17}$$

where τ is defined such that

$$r_a + r_b e^{-\frac{\tau}{T_1}} = 0; \tag{18}$$

i.e., τ is the zero crossing point. Estimates of r_a, r_b, T_1, and τ can then be found as the minimizers of the following fitting criterion:

$$J_\tau = \sum_{n=1}^{N} \left[\gamma_\tau(TI_n) y(TI_n) - \left(r_a + r_b e^{-\frac{TI_n}{T_1}} \right) \right]^2, \tag{19}$$

where the dependence of τ on r_a, r_b, and T_1 should in principle be observed (note from Eq. 18 that $\tau = T_1 \ln(-r_b/r_a)$). However, this minimization problem is rather complicated. To simplify it, reminiscent of (18), we take the *TI* corresponding to the minimum signal

NIH-PA Author Manuscript

NIH-PA Author Manuscript

NIH-PA Author Manuscript

intensity as an approximation of τ. Signal polarity is reversed up to this sampling point, denoted TI_{min}. It then remains to be determined whether the polarity of $y(TI_{min})$ should be reversed. This is done by comparing the minimum values of the criterion in Eq. 19 for $\tau = TI_{min}$ and $\tau = TI_{min+1}$, where the latter refers to the next sampling point after TI_{min} (assuming that $TI_1 < TI_2 < \cdots < TI_N$). We then obtain the following estimates (cf. Appendix B for details):

$$\widehat{\tau}=\arg\min_{\tau\in\{TI_{min},TI_{min+1}\}} J_{\tau}, \tag{20}$$

$$\widehat{T}_1=\arg\max_{T_1}\frac{[\Gamma_{mag}(T_1|\widehat{\tau})]^2}{\Psi(T_1)}, \tag{21}$$

$$\widehat{r}_b=\frac{\Gamma_{mag}(\widehat{T}_1|\widehat{\tau})}{\Psi(\widehat{T}_1)}, \tag{22}$$

$$\widehat{r}_a=\frac{1}{N}\left(\sum_{n=1}^{N}\gamma_{\widehat{\tau}}(TI_n)y(TI_n)-\widehat{r}_b\sum_{n=1}^{N}e^{-\frac{TI_n}{\widehat{T}_1}}\right), \tag{23}$$

where

$$\Gamma_{mag}(T_1|\widehat{\tau})=\sum_{n=1}^{N}e^{-\frac{TI_n}{T_1}}\gamma_{\widehat{\tau}}(TI_n)y(TI_n)-\frac{1}{N}\left(\sum_{n=1}^{N}e^{-\frac{TI_n}{T_1}}\right)\left(\sum_{n=1}^{N}\gamma_{\widehat{\tau}}(TI_n)y(TI_n)\right), \tag{24}$$

and Ψ is defined in Eq. 14. The RD-NLS-PR method thus requires minimizing Eq. 19 two times; i.e., it requires two 1D searches over T_1. Solving Eq. 19 using the LM algorithm requires instead two 3D searches, a computationally more demanding task (16,18).

1.2.3 Grid Search—Using the RD-NLS or RD-NLS-PR approaches proposed here, an estimate of T_1 can be found through a 1D search. Estimates of the other unknowns are then obtained in closed form (Eqs. 11 and 12 or Eqs. 22 and 23). This should be compared with the traditional LM algorithm fit, where the search has to be performed over five dimensions (Eq. 6), over four dimensions (Eq. 3), or over three dimensions (Eq. 3 with magnitude data). There are many algorithms for solving the 1D search problem in Eq. 10; e.g., Newton's method and steepest descent (19). However, as we know the range of possible T_1 estimates, a global grid search can be used. Doing so, there is no need for initialization, and the global optimum is always found. Furthermore, a resolution for T_1 of 1 ms is sufficient (16). We typically searched over $T_1 = \{1, \ldots, 5000\}$ ms. This range can be reduced if a priori information is available.

2 Methods

The novel fitting algorithms were compared to conventional LM algorithms in terms of accuracy, precision, and speed. The respective influence of SNR and T_1 was also

NIH-PA Author Manuscript

NIH-PA Author Manuscript

NIH-PA Author Manuscript

investigated. A robust scanning procedure was then defined. Phantom scans were used to validate the proposed T_1 mapping methodology, and in vivo scans were performed.

2.1 Simulations

2.1.1 Validation of the NLS Algorithms—To compare the conventional LM algorithm and the proposed RD-NLS algorithms, simulations were performed using Matlab 7.5 (The Mathworks, Natick, MA, USA). The data were generated according to Eq. 1, to which circularly Gaussian-distributed, zero-mean, white complex noise with variance σ_n^2 was added. The parameters were set to $\sigma_n = 0.03$, $\theta_1 = 172°$, $\theta_2 = 90°$, $TI = [50\ 400\ 1100\ 2500]$ ms (20, 21), $TR = 2550$ ms, $T_1 = 263$ ms, and $M_0 = 1$. T_1 was then estimated from 20,000 Monte-Carlo simulations, using the RD-NLS and LM algorithms. For the complex data, the LM algorithm was used with both the four-parameter model in Eq. 3 and the five-parameter model in Eq. 6. To initialize the LM algorithms, T_1 was set to 500 ms and the remaining parameters as follows. When fitting the parameters to complex data, with the five-parameter model in Eq. 6, we had $a^{(0)} = S(TI_N)$ and $b^{(0)} = -2a^{(0)}$; i.e., to initialize a and b, we assumed full recovery of the magnetization at the longest sampling point TI. With the four-parameter model in Eq. 3, we did the change of variables $c \triangleq e^{i\phi} r_a$ and $k \triangleq -r_b/r_a$, and we used the LM algorithm to fit the data to the following model:

$$S(TI) = c\left(1 - ke^{-\frac{TI}{T_1}}\right). \tag{25}$$

The LM fit with Eq. 25 was then initialized by setting $c^{(0)} = S(TI_N)$ and $k^{(0)} = 2$. When fitting the parameters to magnitude data, we let $r_a^{(0)} = y(TI_N)$, and $r_b^{(0)} = -2r_a^{(0)}$. The LM fit was performed using both Eq. 16 directly and the polarity restoration method.

2.1.2 Influence of SNR—We simulated data with different σ_n and computed the root mean squared error (RMSE) of the T_1 estimates. 10,000 Monte-Carlo simulations were performed with the same parameters as in Sec. 2.1.1.

2.1.3 Influence of T_1—We performed Monte-Carlo simulations to see how the precision of the T_1 estimation varies with T_1. The same parameters as in Sec. 2.1.1 were used. True T_1 values from 250 ms to 1500 ms spaced by 10 ms were considered, and 10,000 different noise realizations were simulated for each true T_1 value.

2.2 Imaging Protocol

Two sequences were used: a product 2D SE-IR sequence and a 2D GRE-IR sequence that we implemented. Both sequences feature the same 8.64 ms Silver-Hoult adiabatic inversion pulse (22). GRE-IR offers a shorter TE than SE-IR, which can be beneficial for imaging short-T_2 species. With GRE-IR, a fractional echo was used to minimize TE, and magnitude-only images were reconstructed using a homodyne method (23).

With all T_1 mapping methods, several considerations should be kept in mind. Partial volume effects are a concern for in vivo experiments (24). Magnetization transfer (MT) affects the longitudinal relaxation, especially in multi-slice T_1 measurements. In our experiments, we ignored MT effects because of the spacing of the slices and the long TR (25). Finally, T_1 increases with temperature by 2–3% per degree Celsius (26,27). This is usually not a concern for in vivo imaging of healthy volunteers when the core temperature is stable (37°C). However, for phantom and ex vivo imaging, controlling temperature is essential.

NIH-PA Author Manuscript

NIH-PA Author Manuscript

NIH-PA Author Manuscript

2.2.1 Phantom Scans—First, experiments were performed with a 1.5 T GE scanner (GE Healthcare, Milwaukee, WI, USA) on a loading phantom. The GRE-IR sequence and the SE-IR sequence were used successively. The ambient temperature was measured at the beginning and at the end of each scan. A birdcage head coil and the following parameters were used (8): TR = 2550 ms, TE = 14/7 ms (SE/GRE), TI = [50, 400, 1100, 2500] ms, bandwidth (BW) = ±32 kHz, Field-of-View (FOV) = 15 × 15 cm^2, slice thickness = 2 mm, and matrix size = 128 × 128.

2.2.2 Brain Imaging—Our methodology was then applied to brain T_1 mapping of a healthy volunteer at 1.5 T. We complied with the regulations of our institution's human ethics committee. We acquired three slices using the SE-IR sequence, a birdcage head coil, and the following parameters: TR = 2550 ms, TE = 10 ms, TI = [50, 400, 1100, 2500] ms, BW = ±32 kHz, FOV = 24 × 18 cm^2, slice thickness = 5 mm, and matrix size = 128 × 96. Each of the four scans took 4 min 35 sec.

2.2.3 Skin Imaging—Our interest in T_1 mapping was originally triggered by our work in high-resolution skin imaging. High-field (e.g., 7 T) systems are attractive for skin imaging primarily because of the signal gain they provide. In addition, imaging the skin requires small (typically 1-inch-diameter) surface coils to achieve adequate SNR at the desired resolution. For such small coils, body noise dominance is easier to achieve at higher-field strengths (28), which further increases the SNR. Last, wavelength effects—often a concern at high fields—are likely to be negligible because of the small FOV.

One potential concern with higher-field strengths is the increase in T_1 (29), which reduces the SNR efficiency and might offset the SNR benefits of increasing the field strength (30,31). To check if this is indeed the case, we decided to perform skin T_1 mapping at 1.5 T, 3 T, and 7 T.

Skin is composed of three main layers. The outermost layer, the epidermis, is typically 0.1 mm thick. Beneath the epidermis lie the dermis (≈ 1 mm thick) and the hypodermis (≈ 10 mm thick). The epidermis is mainly composed of keratinocytes and the hypodermis of lipids. The dermis is a heterogeneous structure, in which several different types of macromolecules are present. The dermis therefore has short-T_2 components (32,33). Skin temperature depends on the ambient temperature and on perfusion (34).

GE 1.5 T, 3 T, and 7 T scanners with maximum gradient amplitude 40 mT/m and maximum slew rate 150 mT/m/ms were used. Receive-only coils of 1-inch diameter were built and tuned for 1.5 T and 3 T imaging respectively. At 7 T, because there is no body coil, a 1-inch-diameter transmit/receive coil was first built. As muscle T_1 could not be assessed when imaging with the transmit/receive coil (because of its limited sensitivity), a 1-inch-diameter receive-only coil was eventually built and tuned for 7 T, and a Nova quadrature head coil was then adapted to be used as the transmitter (Nova Medical, Wilmington, MA, USA). Both the GRE-IR and the SE-IR sequences were employed, as GRE-IR was expected to give better results in the dermis, where short-T_2 components are present. We acquired two slices using the following parameters: TR = 2550 ms, TE = 14/7 ms (SE/GRE), TI = [50, 400, 1100, 2500] ms, BW = ±32 kHz, FOV = 6 × 6 cm^2, slice thickness = 2 mm and matrix size = 512 × 128. Each scan took 5 min 57 sec. To resolve the different skin layers, the readout direction was usually chosen perpendicular to the skin surface.

The calf of two healthy volunteers was imaged. For each experiment, the subjects were supine with the coil beneath them. Motion can significantly degrade high-resolution skin images (35). To ensure stability, we used padding when imaging with the Nova coil and an Aircast plastic walker boot (DJO, Vista, CA, USA) glued to a heavy plank when imaging

NIH-PA Author Manuscript

NIH-PA Author Manuscript

NIH-PA Author Manuscript

with the body coil. The ambient temperature was measured at the beginning and at the end of each scan.

2.3 Image Processing

Image processing was carried out using Matlab. For the scans, DICOM images with a reconstructed matrix size of 256 × 256 (phantom and brain) or 512 × 512 (skin) were processed. An intensity mask was applied to the images prior to the fit, so that only pixels with sufficient SNR were considered. In vivo, we used region growing to select specific Regions-of-Interest (ROIs) (36). In these ROIs, histograms were computed with a bin size matching the grid size (1 ms). Bins were centered on the grid points and labeled on their center. For the in vivo scans, histograms were smoothed with a 10 ms median filter (37). For the simulation and phantom scans, because the ROIs are homogeneous, T_1 values were fitted to Gaussian distributions. For the in vivo scans, the T_1 value of each tissue was determined as the mode of the histogram and the root mean square deviation about the mode was computed.

The code is available for general use at http://www-mrsrl.stanford.edu/~jbarral/t1map.html.

3 Results

3.1 Simulations

3.1.1 Validation of the NLS Algorithms—Simulations were performed on an IBM X3455 dual Opteron 2220SE with a 2.8 GHz processor and 8 GB RAM. Table 1 presents the results. As can be seen, the RD-NLS and the LM algorithms with phase constraint show very similar performance, both in terms of accuracy; i.e., correct mean, and precision; i.e., variance. For the magnitude data fit, without phase restoration the LM algorithm shows a slightly larger variance. In addition, the RD-NLS algorithms are much faster than the LM algorithms. For the simulated data, the RD-NLS algorithm was 74 times faster than the five-parameter LM algorithm computed with the model in Eq. 6 and 42 times faster than the four-parameter LM algorithm fitted to Eq. 3. For the magnitude data, the RD-NLS-PR was 28 times faster than its corresponding LM algorithm and 14 times faster than the LM algorithm used on Eq. 16.

For the complex data fit we can compute the CRLB, which gives a minimum standard deviation of 11.9. We therefore conclude that the fitting methods are efficient, as the variance has reached the CRLB, and further improvements in terms of variance cannot be gained for this setup.

3.1.2 Influence of SNR—Figure 1a displays the RMSE of the T_1 estimates using the complex data (RD-NLS) and the polarity-restored magnitude data (RD-NLS-PR), together with the CRLB, for different values of the noise standard deviation σ_n. We see that for σ_n = 0.03, which is the noise standard deviation that we used to validate the algorithms, the same results are obtained with both the complex data and the magnitude data. Furthermore, the CRLB is reached. However, for lower SNR, the performance of the estimators degrades, and for $\sigma_n \approx 0.05$, RD-NLS-PR is no longer efficient whereas RD-NLS still is. Using the complex data, the RD-NLS algorithm starts deviating from the CRLB only at $\sigma_n \approx 0.2$. We therefore conclude that for the SNR of the phantom experiments, both methods will perform similarly. For lower SNR, though, using the complex data is beneficial.

3.1.3 Influence of T_1—Figure 1b displays the histograms of T_1 estimates vs. true T_1 values. We see that the larger the true T_1, the larger the standard deviation of the estimate. The smooth increase in standard deviation with T_1 suggests that the exact distribution of

NIH-PA Author Manuscript

NIH-PA Author Manuscript

NIH-PA Author Manuscript

sampling points *TI*s with respect to the true T_1 has little impact on the fitting performance as long as it covers the expected range of T_1 values.

3.2 Phantom Scans

The temperature was 20.7°C at the beginning of the scanning session and 20.2°C at the end of it.

3.2.1 Validation of the NLS Algorithms—The complex data obtained with the SE-IR sequence were fitted using the different algorithms to confirm the Monte-Carlo simulations. Results are presented in Table 2. As was seen with the simulations, all algorithms give similar accuracy and precision, except the LM algorithm without phase restoration for the magnitude data fit, which here shows a slightly lower mean. Moreover, the RD-NLS algorithms show a large benefit in terms of speed over the LM algorithms. RD-NLS is 52 times faster than the five-parameter LM algorithm and 36 times faster than the four-parameter LM algorithm. Regarding the magnitude data, RD-NLS-PR is 30 times faster than the polarity-restored LM algorithm and 34 times faster than the LM algorithm computed using Eq. 16.

3.2.2 Validation of the Pulse Sequences—To compare the two pulse sequences, the complex data obtained with the SE-IR sequence were fitted using the RD-NLS algorithm and the magnitude data obtained with the GRE-IR sequence were fitted using the RD-NLS-PR algorithm. The same ROI comprising 20,464 pixels was used. For the SE-IR data, a mean T_1 estimate of 263 ms and a standard deviation of 12 ms were found. For the GRE-IR data, a mean T_1 estimate of 263 ms and a standard deviation of 10 ms were found.

3.3 Brain Scan

Figure 2 shows the T_1 map of the three brain slices imaged, and Fig. 3 displays the corresponding histogram. Gray matter and white matter were segmented, and their T_1 histograms were computed. T_1 was estimated as 1173 ± 207 ms (29,360 pixels) in gray matter and 653 ± 55 ms (12,135 pixels) in white matter. The sharp cutoff in the histograms is due to the region-growing method that was used for segmentation, with a fixed threshold. More elaborate methods could be used if necessary (38).

3.4 Skin Scans

Figure 4 shows four images obtained at 3 T using a receive-only coil with the SE-IR sequence (only one of the two acquired slices is shown). Figure 5 presents the corresponding map of the *a* parameter (magnitude) and the T_1 map obtained with the RD-NLS algorithm fitting the complex data. The *a* map has contributions from T_2, the proton density, and coil sensitivity. Figure 6 displays the ROIs generated by the region growing procedure (same slice as Fig. 4), and Fig. 7 shows the corresponding histograms (the two slices were aggregated). For each histogram, the mode and root mean square deviation about the mode (σ) are reported.

Table 3 and Fig. 8 summarize the values found. Temperature was steady within 1°C for each experiment, but it varied from 21°C to 23°C between scan sessions. Between 1.5 T and 7 T, dermis T_1 increased by 97%, hypodermis T_1 by 94%, and muscle T_1 by 61%.

NIH-PA Author Manuscript

NIH-PA Author Manuscript

NIH-PA Author Manuscript

4 Discussion

4.1 Fitting Procedure

The proposed RD-NLS fitting algorithms are not only as accurate and precise as LM fitting techniques, but also much faster. Moreover, if additional information about the range of possible T_1 values is available, the search range for the RD-NLS algorithms can be restricted, thereby further decreasing the computing time. Additionally, our approach avoids the delicate task of choosing initial parameters, as it allows for a global search where only the range of possible T_1 values needs to be set. The proposed methods can also be generalized to any T_1 mapping model and to other relaxometry techniques.

In (39), a T_1 estimation method based on VARPRO (40) was proposed. This approach is similar to ours but results in a 2D search and is therefore not as fast. Furthermore, VARPRO was derived for real data, and the approach in (39) is therefore not directly applicable to complex data.

In vivo, T_1 values in different ROIs do not always follow Gaussian distributions. This is partially due to tissue heterogeneity (e.g., for fat) and to coil sensitivity (e.g., for skin imaging).

Note that manually selecting ROIs results in undesirable user-dependent variability. This problem is avoided when region growing is used to define ROIs. Such an approach was found to be simple and robust. The same threshold was used for all maps, and the values obtained were independent of the seed position.

4.2 Phantom Scans

Looking at the respective variance of the complex data fit and the magnitude data fit, good agreement is found between the phantom scans (Table 2) and the simulations (Table 1).

Owing to its shorter TE, the GRE-IR sequence provides data with an improved SNR and therefore a better precision than the SE-IR sequence.

4.3 Brain Scan

The gray matter value found (1173 ms) is in agreement with the value found by Stanisz et al. ex vivo (1124 ms). The white matter value found (653 ms), however, is significantly lower than his (884 ms) (41). Our value is in good agreement with values reported by Kingsley et al. in vivo (636 in frontal white matter and 648 in occipital white matter) (7). As already mentioned, values reported in the literature span a wide range (2). As a relatively low resolution was used and partial volume effects are not accounted for by our simple segmentation method, a large variance is observed in the T_1 estimates.

4.4 Skin Scans

As the hypodermis has the highest SNR (Fig. 5a) and the shortest T_1 value, it also presents the lowest variance (Fig. 1). The dermis is a heterogeneous layer, and a broad range of T_1 values is found in the histogram of the dermis at all field strengths.

When comparing across experiments at a given field strength, we find reasonable agreement between the two sequences used, GRE-IR and SE-IR. The observed differences can be explained by physiological variations between the two scan sessions (temperature, perfusion), T_2^* signal loss with GRE-IR, or sensitivity to different T_2 components because a shorter TE is used with GRE-IR (33). In addition, since a fractional echo is used with GRE-

NIH-PA Author Manuscript

NIH-PA Author Manuscript

NIH-PA Author Manuscript

IR, only magnitude data are available, which might degrade the fitting performance if SNR is low.

In the early days of skin imaging, Richard et al. reported T_1 values of 870 ms in the dermis and 393 ms in the hypodermis (32), when scanning the calf at 1.5 T. We found significantly lower values. Our values are in good agreement with those reported by Stanisz et al. (41) for muscle and those reported by Gold et al. (42) for hypodermis (subcutaneous fat) and muscle. The large variance found in muscle can be attributed to tissue heterogeneity, partial volume effects, or the natural variability between different muscle tissues.

We conclude that the T_1 increase slightly attenuates the SNR benefits of increasing the field strength but is far from offsetting them.

4.5 Limitations

The main limitation of our approach is the scanning procedure: 24 min were typically required to collect the skin data. Since our novel fitting procedures can be used with any T_1 mapping method, we believe that the long protocol should be used as a gold standard to validate faster scanning procedures on phantoms, before using the faster techniques in vivo. Note that when imaging phantoms, monitoring temperature is critical.

For skin, the protocol was chosen to be applicable at the three field strengths considered. However, if a single field strength is used, the protocol could be adapted. In particular, the limits of the protocol used in this work are reached at 7 T: chemical shift displaces fat by 8 pixels, aliasing is a concern, and scanner drift might become an issue.

Conclusion

We have introduced a robust methodology for T_1 mapping consisting of a gold standard scanning procedure and a novel fitting procedure.

The data, either magnitude data or complex data, were fitted to a five-parameter model. We proposed a reduced-dimension nonlinear least squares fitting algorithm, which was shown to be accurate, precise, and fast. Our algorithm can be adapted to fit data to any T_1 mapping model.

Acknowledgments

This work was supported by the NIH (1R01 HL075803), GE Healthcare, the Swedish Foundation for International Cooperation in Research and Higher Education (STINT), the Swedish Research Council (VR), and the European Research Council (ERC).

The authors thank Steven Conolly, Mariya Doneva, and Jason Hsu for insightful discussions and Mohammad-Mehdi Khalighi for help with the coil setup at 7 T.

APPENDIX A– Derivation of the CRLBs for the different models

Let φ denote a vector containing the unknown parameters and assume that the additive noise is a circularly Gaussian-distributed, zero-mean, white complex process with variance σ_n^2. The Fisher information matrix (FIM) can then be expressed, using the Slepian-Bang formula (13), as

$$\mathrm{FIM}=\frac{2}{\sigma_n^2}\sum_{n=1}^{N}\mathrm{Re}\left\{\left(\frac{\partial S(TI_n)}{\partial\varphi}\right)\left(\frac{\partial S(TI_n)}{\partial\varphi}\right)^{*}\right\}, \qquad \text{(A-1)}$$

NIH-PA Author Manuscript

NIH-PA Author Manuscript

NIH-PA Author Manuscript

where x^* and $\mathrm{Re}\{x\}$ denote the conjugate of x and the real part of x, respectively. The CRLB is then given by the diagonal elements of the inverse of the FIM.

The Four-Parameter Models

The Model in Eq. 3

From Eq. 3, $\varphi = [\phi\ r_a\ r_b\ T_1]^T$, so the FIM is a 4 × 4 matrix containing the partial derivatives

$$\frac{\partial S(TI)}{\partial \phi} = ie^{i\phi}\left(r_a + r_b e^{-\frac{TI}{T_1}}\right), \quad \frac{\partial S(TI)}{\partial r_b} = e^{i\phi}e^{-\frac{TI}{T_1}},$$
$$\frac{\partial S(TI)}{\partial r_a} = e^{i\phi}, \quad \frac{\partial S(TI)}{\partial T_1} = e^{i\phi}r_b T_1^{-2} TI e^{-\frac{TI}{T_1}}.$$

We perform the inversion of the FIM using Matlab's Symbolic Math Toolbox and we obtain the following analytical expression for the CRLB of T_1:

$$\begin{aligned}\mathrm{CRLB}(T_1) &= [\mathrm{FIM}^{-1}]_{44} \\ &= \frac{\sigma_n^2(S_1^2 - NS_2)}{2r_b^2 T_1^{-4}(S_1^2 S_{22} - 2S_1 S_{12} S_{11} - NS_2 S_{22} + NS_{12}^2 + S_2 S_{11}^2)},\end{aligned} \tag{A-2}$$

where

$$\begin{aligned} S_1 &= \sum_{n=1}^{N} e^{-\frac{TI_n}{T_1}}, \quad & S_2 &= \sum_{n=1}^{N} e^{-\frac{2TI_n}{T_1}}, \\ S_{11} &= \sum_{n=1}^{N} TI_n e^{-\frac{TI_n}{T_1}}, \quad & S_{12} &= \sum_{n=1}^{N} TI_n e^{-\frac{2TI_n}{T_1}}, \\ S_{22} &= \sum_{n=1}^{N} TI_n^2 e^{-\frac{2TI_n}{T_1}}. \end{aligned} \tag{A-3}$$

The Model in Eq. 7

From Eq. 7, $\varphi = [c_R\ c_I\ \theta_1\ T_1]^T$, where $c_R = \mathrm{Re}\{c\}$ and $c_I = \mathrm{Im}\{c\}$: this is just a change of coordinates from the model in Eq. 3. The CRLB of T_1 derived from Eq. 7 is thus identical to that in Eq. A-2.

The Five-Parameter Model

Equation 6 gives $\varphi = [a_R\ a_I\ b_R\ b_I\ T_1]^T$, where $a_R = \mathrm{Re}\{a\}$, $a_I = \mathrm{Im}\{a\}$, $b_R = \mathrm{Re}\{b\}$, and $b_I = \mathrm{Im}\{b\}$. The FIM for the five-parameter model is therefore a 5 × 5 matrix containing the partial derivatives

$$\begin{aligned} \frac{\partial S(TI)}{\partial a_R} &= 1, & \frac{\partial S(TI)}{\partial b_R} &= e^{-\frac{TI}{T_1}}, \\ \frac{\partial S(TI)}{\partial a_I} &= i, & \frac{\partial S(TI)}{\partial b_I} &= ie^{-\frac{TI}{T_1}}, \\ \frac{\partial S(TI)}{\partial T_1} &= bT_1^{-2} TI e^{-\frac{TI}{T_1}}. \end{aligned} \tag{A-4}$$

We use the Symbolic Math Toolbox in Matlab to compute the inverse of the FIM and we obtain

NIH-PA Author Manuscript

NIH-PA Author Manuscript

NIH-PA Author Manuscript

$$\begin{aligned}\mathrm{CRLB}(T_1) &= [\mathrm{FIM}^{-1}]_{55} \\ &= \frac{\sigma_n^2(S_1^2 - NS_2)}{2|b|^2 T_1^{-4}(S_1^2 S_{22} - 2S_1 S_{12} S_{11} - NS_2 S_{22} + NS_{12}^2 + S_2 S_{11}^2)},\end{aligned} \tag{A-5}$$

where S_1, S_2, S_{11}, S_{12}, and S_{22} are defined in Eq. A-3. We note that this CRLB is identical to that of the four-parameter models (Eq. A-2).

APPENDIX B – Derivation of the RD-NLS Algorithms

Complex Data

Expanding Eq. 9 yields

$$J_1 = \sum_{n=1}^{N} |S(TI_n)|^2 - 2\sum_{n=1}^{N} \mathrm{Re}\left\{S^*(TI_n)\left(a + be^{-\frac{TI_n}{T_1}}\right)\right\} + \sum_{n=1}^{N}\left|a + be^{-\frac{TI_n}{T_1}}\right|^2. \tag{B-1}$$

By further expanding and by completing the square we get the following expression for J_1:

$$J_1 = f_1(S(TI)) + N\left|a - \frac{1}{N}\left(\sum_{n=1}^{N} S(TI_n) - b\sum_{n=1}^{N} e^{-\frac{TI_n}{T_1}}\right)\right|^2 + \left|b - \frac{\Gamma(T_1)}{\Psi(T_1)}\right|^2\left[\sum_{n=1}^{N} e^{-\frac{2TI_n}{T_1}} - \frac{1}{N}\left(\sum_{n=1}^{N} e^{-\frac{TI_n}{T_1}}\right)^2\right] - \frac{|\Gamma(T_1)|^2}{\Psi(T_1)}, \tag{B-2}$$

where $f_1(S(TI))$ denotes a function that depends only on the data, and $\Gamma(T_1)$ and $\Psi(T_1)$ are defined in Eqs. 13 and 14, respectively. The minimizer of J_1 with respect to a and b is thus given by

$$\widehat{a} = \frac{1}{N}\left(\sum_{n=1}^{N} S(TI_n) - b\sum_{n=1}^{N} e^{\frac{TI_n}{T_1}}\right), \tag{B-3}$$

$$\widehat{b} = \frac{\Gamma(T_1)}{\Psi(T_1)}. \tag{B-4}$$

Inserting Eqs. B-3 and B-4 in B-2 then yields the following optimal estimate of T_1:

$$\widehat{T}_1 = \arg\max_{T_1} \frac{|\Gamma(T_1)|^2}{\Psi(T_1)}. \tag{B-5}$$

Magnitude Data

We expand Eq. 19 similarly to the case of complex data, which gives

$$J_\tau = \sum_{n=1}^{N} [\gamma_\tau(TI_n) y(TI_n)]^2 - 2\sum_{n=1}^{N} \gamma_\tau(TI_n) y(TI_n)\left(r_a + r_b e^{-\frac{TI_n}{T_1}}\right) + \sum_{n=1}^{N}\left(r_a + r_b e^{-\frac{TI_n}{T_1}}\right)^2. \tag{B-6}$$

NIH-PA Author Manuscript

NIH-PA Author Manuscript

NIH-PA Author Manuscript

Again, this can be further expanded and we obtain the following minimization criterion:

$$\begin{aligned} J_\tau = & f_2(\gamma_\tau(TI)y(TI)) \\ & + N\left[r_a - \frac{1}{N}\left(\sum_{n=1}^{N} \gamma_\tau(TI_n)y(TI_n) - r_b \sum_{n=1}^{N} e^{-\frac{TI_n}{T_1}} \right) \right]^2 \\ & + \left[r_b - \frac{\Gamma(T_1|\tau)}{\Psi(T_1)} \right]^2 \left[\sum_{n=1}^{N} e^{-\frac{2TI_n}{T_1}} - \frac{1}{N}\left(\sum_{n=1}^{N} e^{-\frac{TI_n}{T_1}} \right)^2 \right] \\ & - \frac{[\Gamma(T_1|\tau)]^2}{\Psi(T_1)}, \end{aligned} \tag{B-7}$$

where $f_2(\gamma_\tau(TI)y(TI))$ is a function that depends only on the data, and $\Gamma(T_1|\tau)$ and $\Psi(T_1)$ are defined in Eqs. 24 and 14, respectively. For a given τ, the minimizer of J_τ with respect to r_a and r_b is thus given by

$$\widehat{r_a} = \frac{1}{N}\left(\sum_{n=1}^{N} \gamma_\tau(TI_n)y(TI_n) - r_b \sum_{n=1}^{N} e^{\frac{TI_n}{T_1}} \right), \tag{B-8}$$

$$\widehat{r_b} = \frac{\Gamma(T_1|\tau)}{\Psi(T_1)}, \tag{B-9}$$

which, re-inserted in Eq. B-7, gives the following optimal estimate of T_1:

$$\widehat{T_1} = \arg\max_{T_1} \frac{[\Gamma_{mag}(T_1|\tau)]^2}{\Psi(T_1)}. \tag{B-10}$$

This is done for $\tau = TI_{min}$ and $\tau = TI_{min+1}$, and an approximation of τ is found as

$$\widehat{\tau} = \arg\min_{\tau \in \{TI_{min}, TI_{min+1}\}} J_\tau, \tag{B-11}$$

which, reinserted in Eq. B-10, provides an estimate of T_1.

References

1. Kingsley PB. Methods of measuring spin-lattice (T_1) relaxation times: An annotated bibliography. Concepts Magn Reson. 1999; 11:243–276.
2. Tofts, P. Quantitative MRI of the brain: measuring changes caused by disease. West Sussex: Wiley, Chichester; 2003.
3. Drain LE. A direct method of measuring nuclear spin-lattice relaxation times. Proc Phys Soc Lond A. 1949; 62:301.
4. Hahn EL. An accurate nuclear magnetic resonance method for measuring spin-lattice relaxation times. Phys Rev. 1949; 76:145–146.
5. Bevington, PR. Data reduction and error analysis for the physical sciences. New York: McGraw-Hill; 1969. pp. 235–236

NIH-PA Author Manuscript

NIH-PA Author Manuscript

NIH-PA Author Manuscript

6. Gupta R, Ferretti J, Becker E, Weiss G. A modified fast inversion-recovery technique for spin-lattice relaxation measurements. J Magn Reson. 1980; 38:447–452.
7. Kingsley PB, Ogg RJ, Reddick WE, Steen RG. Correction of errors caused by imperfect inversion pulses in MR imaging measurement of T_1 relaxation times. Magn Reson Imaging. 1998; 16:1049–1055. [PubMed: 9839989]
8. Weiss G, Gupta RK, Ferretti J, Becker E. The choice of optimal parameters for measurement of spin lattice relaxation times. J Magn Reson. 1980; 37:369–379.
9. Crawley AP, Henkelman RM. A comparison of one-shot and recovery methods in T_1 imaging. Magn Reson Med. 1988; 7:23–34. [PubMed: 3386519]
10. MacFall JR, Wehrli FW, Breger RK, Johnson GA. Methodology for the measurement and analysis of relaxation times in proton imaging. Magn Reson Imaging. 1987; 5:209–220. [PubMed: 3041152]
11. Frank LR, Wong EC, Buxton RB. Slice profile effects in adiabatic inversion: application to multislice perfusion imaging. Magn Reson Med. 1997; 38:558–564. [PubMed: 9324322]
12. Young IR, Bryant DJ, Payne JA. Variations in slice shape and absorption as artifacts in the determination of tissue parameters in NMR imaging. Magn Reson Med. 1985; 2:355–389. [PubMed: 4094552]
13. Stoica, P.; Moses, R. Spectral analysis of signals. Upper Saddle River, N.J.: Prentice Hall; 2005.
14. Ahn CB, Cho ZH. A new phase correction method in NMR imaging based on autocorrelation and histogram analysis. IEEE Trans Med Imaging. 1987; 6:32–36. [PubMed: 18230424]
15. Gowland PA, Leach MO. A simple method for the restoration of signal polarity in multi-image inversion recovery sequences for measuring T_1. Magn Reson Med. 1991; 18:224–231. [PubMed: 2062234]
16. Nekolla S, Gneiting T, Syha J, Deichmann R, Haase A. T_1 maps by K-space reduced snapshot-FLASH MRI. J Comput Assist Tomogr. 1992; 16:327–332. [PubMed: 1545039]
17. Bernstein, M.; King, K.; Zhou, ZJ. Handbook of MRI pulse sequences. Amsterdam: Academic Press; 2004. chapter 14.2 Inversion Recovery; p. 616-620.
18. Bakker CG, DeGraaf CN, VanDijk P. Restoration of signal polarity in a set of inversion recovery NMR images. IEEE Trans Med Imaging. 1984; 3:197–202. [PubMed: 18234630]
19. Boyd, S.; Vandenberghe, L. Cambridge, UK: Cambridge University Press; 2004. Convex Optimization.
20. Zhang Y, Yeung HN, O'Donnell M, Carson PL. Determination of sample time for T_1 measurement. J Magn Reson Imaging. 1998; 8:675–681. [PubMed: 9626885]
21. Ogg RJ, Kingsley PB. Optimized precision of inversion-recovery T_1 measurements for constrained scan time. Magn Reson Med. 2004; 51:625–630. [PubMed: 15004808]
22. Silver MS, Joseph RI, Hoult DI. Highly selective $\pi/2$ and π pulse generation. J Magn Reson. 1984; 59:347–351.
23. Noll DC, Nishimura DG, Macovski A. Homodyne detection in magnetic resonance imaging. IEEE Trans Med Imaging. 1991; 10:154–163. [PubMed: 18222812]
24. Rakow-Penner R, Daniel B, Yu H, Sawyer-Glover A, Glover GH. Relaxation times of breast tissue at 1.5T and 3T measured using IDEAL. J Magn Reson Imaging. 2006; 23:87–91. [PubMed: 16315211]
25. Graham SJ, Henkelman RM. Pulsed magnetization transfer imaging: evaluation of technique. Radiology. 1999; 212:903–910. [PubMed: 10478264]
26. Lewa C, Majewska Z. Temperature relationships of proton spin-lattice relaxation times T_1 in biological tissues. Bull Cancer. 1980; 67:525–530. [PubMed: 6260272]
27. Nelson TR, Tung SM. Temperature dependence of proton relaxation times in vitro. Magn Reson Imaging. 1987; 5:189–199. [PubMed: 3041151]
28. Doty F, Entzminger G, Kulkarni J, Pamarthy K, Staab J. Radio frequency coil technology for small-animal MRI. NMR Biomed. 2007; 20:304–325. [PubMed: 17451180]
29. Bottomley PA, Foster TH, Argersinger RE, Pfeifer LM. A review of normal tissue hydrogen NMR relaxation times and relaxation mechanisms from 1–100 MHz: dependence on tissue type, NMR

NIH-PA Author Manuscript

NIH-PA Author Manuscript

NIH-PA Author Manuscript

frequency, temperature, species, excision, and age. Med Phys. 1984; 11:425–448. [PubMed: 6482839]

30. Hoult DI, Chen CN, Sank VJ. The field dependence of NMR imaging. II. Arguments concerning an optimal field strength. Magn Reson Med. 1986; 3:730–746. [PubMed: 3784890]
31. Redpath TW. Signal-to-noise ratio in MRI. Brit J Radiol. 1998; 71:704–707. [PubMed: 9771379]
32. Richard S, Querleux B, Bittoun J, Idy-Peretti I, Jolivet O, Cermakova E, Leveque JL. In vivo proton relaxation times analysis of the skin layers by magnetic resonance imaging. J Invest Dermatol. 1991; 97:120–125. [PubMed: 2056181]
33. Song HK, Wehrli FW, Ma J. In vivo MR microscopy of the human skin. Magn Reson Med. 1997; 37:185–191. [PubMed: 9001141]
34. Agache, P. Measuring the Skin. Springer; 2004. chapter 38: Thermometry and Remote Thermography.
35. Barral JK, Bangerter NK, Hu BS, Nishimura DG. In vivo high-resolution magnetic resonance skin imaging at 1.5 T and 3 T. Magn Reson Med. 2010; 63:790–796. [PubMed: 20146351]
36. Gonzalez, RC.; Woods, RE. Digital image processing. 3rd ed. Upper Saddle River, N.J.: Prentice Hall; 2008.
37. Tofts PS, Steens SCA, Cercignani M, Admiraal-Behloul F, Hofman PAM, van Osch MJP, Teeuwisse WM, Tozer DJ, van Waesberghe JHTM, Yeung R, Barker GJ, van Buchem MA. Sources of variation in multi-centre brain MTR histogram studies: body-coil transmission eliminates inter-centre differences. MAGMA. 2006; 19:209–222. [PubMed: 16957936]
38. Zhang Y, Brady M, Smith S. Segmentation of brain MR images through a hidden Markov random field model and the expectation-maximization algorithm. IEEE Trans Med Imaging. 2001; 20:45–57. [PubMed: 11293691]
39. Haldar, JP.; Anderson, J.; Sun, SW. Maximum likelihood estimation of T_1 relaxation parameters using VARPRO; Proceedings of the 15th Annual Meeting of ISMRM; Berlin, Germany. 2007. p. 41
40. Golub GH, Pereyra A. The differentiation of pseudo-inverses and nonlinear least squares problems whose variables separate. SIAM J Numer Anal. 1973; 10:413–432.
41. Stanisz GJ, Odrobina EE, Pun J, Escaravage M, Graham SJ, Bronskill MJ, Henkel-man RM. T_1, T_2 relaxation and magnetization transfer in tissue at 3T. Magn Reson Med. 2005; 54:507–512. [PubMed: 16086319]
42. Gold GE, Han E, Stainsby J, Wright G, Brittain J, Beaulieu C. Musculoskeletal MRI at 3.0 T: relaxation times and image contrast. Am J Roentgenol. 2004; 183:343–351. [PubMed: 15269023]

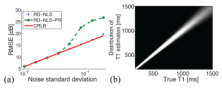

Figure 1.

Influence of SNR and T_1. (a) RMSE of the T_1 estimates using the complex data (RD-NLS) and the polarity-restored magnitude data (RD-NLS-PR), together with the CRLB, for different σ_n. (b) T_1 estimates as a function of true T_1 values. Each column gives a histogram of the T_1 estimate distribution for a given true T_1. The precision worsens as the true T_1 increases.

NIH-PA Author Manuscript
NIH-PA Author Manuscript
NIH-PA Author Manuscript

NIH-PA Author Manuscript
NIH-PA Author Manuscript
NIH-PA Author Manuscript

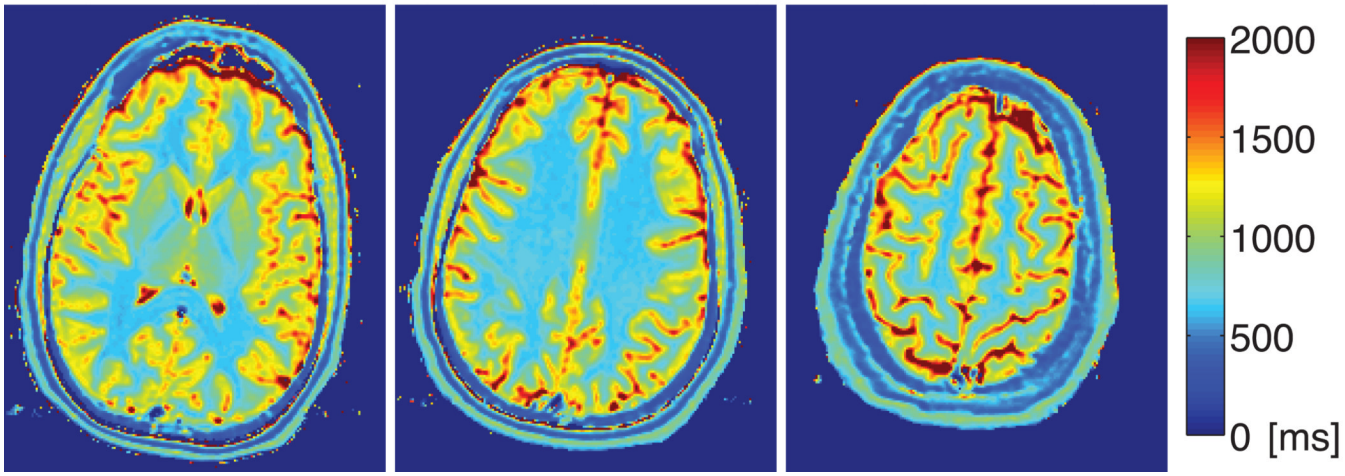

Figure 2.
Brain T_1 maps at 1.5 T. Three slices were imaged and the RD-NLS algorithm was used on the complex data.

NIH-PA Author Manuscript

NIH-PA Author Manuscript

NIH-PA Author Manuscript

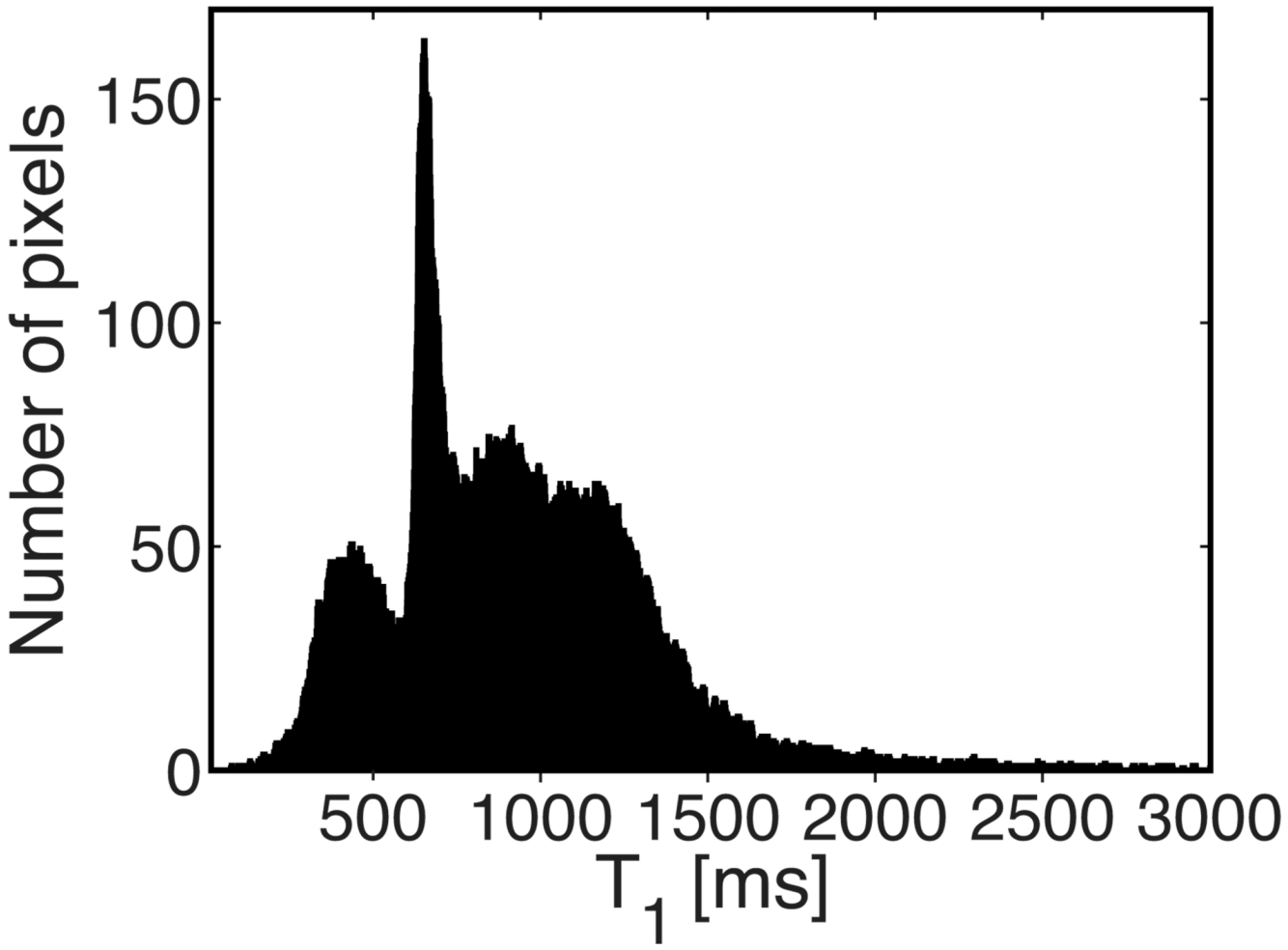

Figure 3.
Brain T_1 histogram. The three imaged slices were aggregated. Peaks corresponding to white matter (653 ms) and gray matter (1173 ms) are visible. The leftmost peak corresponds to skull and is segmented out when ROIs are specified.

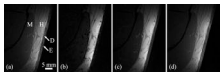

Figure 4.
Skin images obtained at 3 T with the SE-IR sequence. Inversion times are (a) 50 ms, (b) 400 ms, (c) 1100 ms, and (d) 2500 ms. The following structures can be recognized: E: epidermis; D: dermis; H: hypodermis; M: muscle.

NIH-PA Author Manuscript
NIH-PA Author Manuscript
NIH-PA Author Manuscript

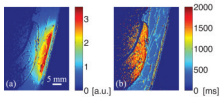

Figure 5.

(a) Map of the *a* parameter (magnitude) and (b) T_1 map obtained at 3 T with the SE-IR sequence. The *a* map has contributions from T_2, proton density, and coil sensitivity. The dermis has a low proton density and a short T_2 (32). The coil sensitivity drops as the distance from the skin surface increases. The T_1 map shows the dermis heterogeneity.

NIH-PA Author Manuscript NIH-PA Author Manuscript NIH-PA Author Manuscript

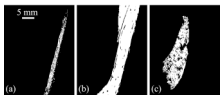

Figure 6.
ROI in (a) dermis, (b) hypodermis, and (c) muscle. Hypodermis and muscle are segmented using a region growing algorithm. The threshold used is the same for hypodermis and muscle, and the ROIs are independent of the seed position. The dermis is obtained by subtraction, and therefore includes the epidermis.

NIH-PA Author Manuscript
NIH-PA Author Manuscript
NIH-PA Author Manuscript

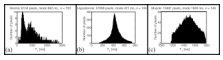

Figure 7.
Histograms obtained in (a) dermis, (b) hypodermis, and (c) muscle at 3 T with the SE-IR sequence. σ is the root mean square deviation about the mode.

NIH-PA Author Manuscript
NIH-PA Author Manuscript
NIH-PA Author Manuscript

NIH-PA Author Manuscript

NIH-PA Author Manuscript

NIH-PA Author Manuscript

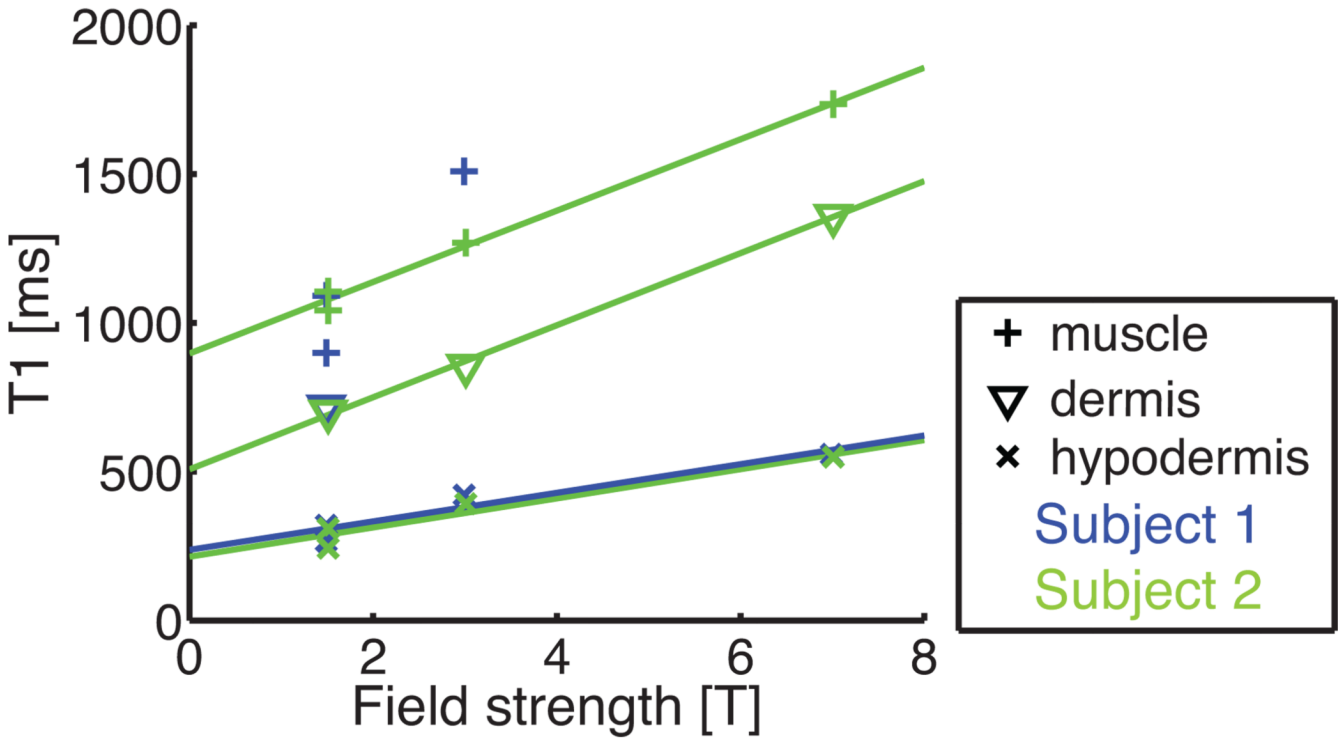

Figure 8.
Dispersion plot obtained from Table 3. For the hypodermis, T_1 depends linearly on the field strength. A linear trend is also observed in dermis and muscle, but variability is more pronounced.

NIH-PA Author Manuscript

NIH-PA Author Manuscript

NIH-PA Author Manuscript

Table 1

Monte-Carlo Simulations (20,000 pixels): (top) complex and (bottom) magnitude data fits with the RD-NLS and LM algorithms (mean μ, standard deviation σ, and processing time are given). T_1 = 263 ms was used to generate the data.

Algorithm (model)	μ [ms]	σ [ms]	Time [min:sec]
LM (five-parameter)	263	12	13:39
LM (four-parameter)	263	12	7:39
RD-NLS (five-parameter)	263	12	0:11

Algorithm (model)	μ [ms]	σ [ms]	Time [min:sec]
LM (three-parameter)	263	13	3:52
LM-PR (three-parameter)	263	12	7:32
RD-NLS-PR (three-parameter)	263	12	0:16

NIH-PA Author Manuscript

NIH-PA Author Manuscript

NIH-PA Author Manuscript

Table 2

Phantom SE-IR Scan (20,719 pixels): (top) complex and (bottom) magnitude data fits with the RD-NLS and LM algorithms (mean μ, standard deviation σ, and processing time are given).

Algorithm (model)	μ [ms]	σ [ms]	Time [min:sec]
LM (five-parameter)	263	12	9:40
LM (four-parameter)	263	12	6:37
RD-NLS (five-parameter)	263	12	0:11

Algorithm (model)	μ [ms]	σ [ms]	Time [min:sec]
LM (three-parameter)	262	12	9:28
LM-PR (three-parameter)	263	12	8:18
RD-NLS-PR (three-parameter)	263	12	0:17

NIH-PA Author Manuscript NIH-PA Author Manuscript NIH-PA Author Manuscript

Table 3

Skin scans: T_1 values (in ms) found in dermis, hypodermis, and muscle at 1.5 T, 3 T, and 7 T (mode ± root mean square deviation about the mode (number of pixels)). NA means that the corresponding value was Not Available. Muscle values could not be assessed when a transmit/receive (Tx-Rc) coil was used, because of the limited sensitivity. Dermis T_1 was hard to determine because of tissue heterogeneity, and values were not reported when the distribution had more than one peak, due to partial volume effects (e.g., Fig. 7a).

Subject	Sequence	Field	Coil	T_1 dermis	T_1 hypodermis	T_1 muscle
1	SE-IR	1.5	Rc	NA	320 ± 89 (67,120)	899 ± 183 (50,584)
1	GRE-IR	1.5	Rc	718 ± 347 (6,865)	266 ± 72 (51,091)	1091 ± 158 (19,168)
2	SE-IR	1.5	Rc	701 ± 304 (2,466)	309 ± 102 (32,872)	1042 ± 163 (87,528)
2	GRE-IR	1.5	Rc	NA	243 ± 82 (19,286)	1105 ± 154 (56,977)
1	SE-IR	3	Rc	NA	421 ± 104 (57,089)	1509 ± 150 (20,521)
2	SE-IR	3	Rc	855 ± 546 (12,281)	392 ± 132 (24,688)	1269 ±141 (93,202)
1	SE-IR	7	Tx- Rc	NA	558 ±115 (27,539)	NA
2	SE-IR[1]	7	Rc	1359 ± 487 (4,272)	549±138 (11,546)	1735±178 (27,741)

[1] The readout direction was chosen parallel to the skin surface for this experiment.